2009

# The Effect of Wind–Wave–Current Interaction on Air–Sea Momentum Fluxes and Ocean Response in Tropical Cyclones

Yalin Fan
*University of Rhode Island*

Isaac Ginis
*University of Rhode Island*, iginis@uri.edu

Tetsu Hara
*University of Rhode Island*, thara@uri.edu



## Citation/Publisher Attribution

Fan, Y., I. Ginis, and T. Hara, 2009: The Effect of Wind–Wave–Current Interaction on Air–Sea Momentum Fluxes and Ocean Response in Tropical Cyclones. *J. Phys. Oceanogr.,* **39**, 1019–1034, https://doi.org/10.1175/2008JPO4066.1
Available at: https://doi.org/10.1175/2008JPO4066.1

# The Effect of Wind–Wave–Current Interaction on Air–Sea Momentum Fluxes and Ocean Response in Tropical Cyclones

# The Effect of Wind–Wave–Current Interaction on Air–Sea Momentum Fluxes and Ocean Response in Tropical Cyclones

YALIN FAN, ISAAC GINIS, AND TETSU HARA

*Graduate School of Oceanography, University of Rhode Island, Narragansett, Rhode Island*

(Manuscript received 12 June 2008, in final form 16 September 2008)

ABSTRACT

In this paper, the wind–wave–current interaction mechanisms in tropical cyclones and their effect on the surface wave and ocean responses are investigated through a set of numerical experiments. The key element of the authors' modeling approach is the air–sea interface model, which consists of a wave boundary layer model and an air–sea momentum flux budget model. The results show that the time and spatial variations in the surface wave field, as well as the wave–current interaction, significantly reduce momentum flux into the currents in the right rear quadrant of the hurricane. The reduction of the momentum flux into the ocean consequently reduces the magnitude of the subsurface current and sea surface temperature cooling to the right of the hurricane track and the rate of upwelling/downwelling in the thermocline. During wind–wave–current interaction, the momentum flux into the ocean is mainly affected by reducing the wind speed relative to currents, whereas the wave field is mostly affected by refraction due to the spatially varying currents. In the area where the current is strongly and roughly aligned with wave propagation direction, the wave spectrum of longer waves is reduced, the peak frequency is shifted to a higher frequency, and the angular distribution of the wave energy is widened.

## 1. Introduction

The passage of a tropical cyclone (TC) over a warm ocean represents one of the most extreme cases of air–sea interaction. The most apparent effects of TC passage are marked sea surface temperature (SST) cooling of 1° to 5°C, strong current velocities of more than 2 m $s^{-1}$, and large surface gravity waves. It is well established that the intensity of a TC over an open ocean may be significantly affected by the cooling of SST caused by air–sea interaction (Khain and Ginis 1991; Schade and Emanuel 1999; Cione and Uhlhorn 2003; Ren and Perrie 2006). Three-dimensional coupled atmosphere–ocean research and operational models have been developed to simulate and predict the mutual response of a TC and the ocean (Ginis et al. 1989; Bender and Ginis 2000; Bender et al. 1993; Bao et al. 2000; Bender et al. 2007; Chen et al. 2007; Surgi 2007). One such coupled model, the Geophysical Fluid Dynamics Laboratory–University of Rhode Island (GFDL/URI) hurricane–ocean prediction system, has been used operationally at the NOAA National Centers for Environmental Prediction (NCEP) since 2001 (Bender et al. 2007). The GFDL/URI model has demonstrated steady improvements in TC intensity prediction over the last several years. Another fully coupled model, the Hurricane Weather Research and Forecast (HWRF) model, became operational at NCEP in 2007 (Surgi 2007).

Previous numerical modeling studies of the ocean response to TCs (Price 1981; Ginis and Dikinov 1989; Jacob et al. 2000; Morey et al. 2006) pointed out that the major factor that governs the SST response to hurricanes is the momentum flux at the sea surface. Although many experimental and theoretical studies have shown that momentum flux is strongly dependent on the wave-induced processes near the ocean surface (Drennan et al. 2003; Hara and Belcher 2004; Moon et al. 2004a,b; Fan et al. 2008a, manuscript submitted to *J. Geophys. Res.,* hereafter FanA; Fan et al. 2008b, manuscript submitted to *J. Geophys. Res.,* hereafter FanB), the role of wind–wave–current coupled processes is not well understood and therefore often ignored.

Proper evaluation of the sea state dependence of air–sea fluxes requires modeling the wave boundary layer (lower part of the atmospheric boundary layer that is

*Corresponding author address:* Yalin Fan, Graduate School of Oceanography, University of Rhode Island, Narragansett, RI 02882.
E-mail: yalin@gso.uri.edu

DOI: 10.1175/2008JPO4066.1

affected by surface waves) and the equilibrium range of wave spectra. Based on the equilibrium wave spectrum model by Hara and Belcher (2002), Hara and Belcher (2004) developed a wave boundary layer model and estimated the air–sea momentum flux over fully developed seas by explicitly calculating the form drag due to nonbreaking waves. Moon et al. (2004a,b) have coupled the NOAA wave model, WAVEWATCH III (WWIII), the equilibrium wave spectrum model, and the wave boundary layer model to predict the air–sea momentum fluxes over any given surface wave fields, including those under TCs. Their results show that the drag coefficient is spatially variable and is generally reduced at very high wind speeds under TCs, consistent with field observations (Black et al. 2007).

Traditionally, the momentum and turbulent kinetic energy (TKE) fluxes from wind to waves are assumed to be identical to the flux into subsurface currents due to wave breaking, based on the assumption that no net momentum (or TKE) is gained (or lost) by surface waves. This assumption, however, is invalid when the surface wave field is not fully developed. Especially under TC conditions, the surface wave field is complex and fast varying in space and time, and may significantly affect the air–sea flux budget. Typically used in ocean models, bulk parameterizations of air–sea fluxes (Fan et al. 2005) assume that 1) the momentum and TKE fluxes are independent of the sea state and no net momentum and TKE is gained (or lost) by surface waves and 2) the effect of wave–current interaction is negligible on both the ocean current and surface gravity wave fields. FanA and FanB investigated the effect of surface gravity waves on the momentum and TKE transfer budget across the air–sea interface under growing seas and TC conditions. They found that the momentum and TKE fluxes into ocean currents could be significantly less than the fluxes from air when the wave field is growing and extracting momentum and TKE, particularly in the right rear quadrant of the TC. In an idealized TC with maximum wind speed of 45 m $s^{-1}$ moving with a forward speed of 5 m $s^{-1}$, this reduction is up to 6% for the momentum flux and 9% for the TKE flux on the right side of the storm. This difference highlights the significance of the air–sea flux budget analysis in coupled models.

Theoretical (Kenyon and Sheres 2006) and numerical (Tolman et al. 1996) studies have pointed out that, if the ocean currents have a large horizontal gradient, they may significantly affect the surface gravity wave field. Since strong surface currents with large horizontal gradients are typically observed under TC forcing, wave–current interaction can be important in the air–sea interaction processes during TCs. The strong TC-induced ocean currents may also affect the momentum flux into the currents due to the difference between the wind and the current.

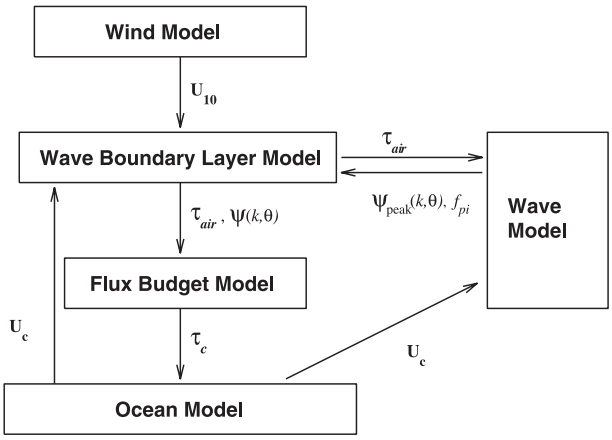


FIG. 1. A schematic diagram of the coupled wind–wave–ocean model (experiment D). The arrows indicate the prognostic variables that are passed between the model components. Here, $\mathbf{U}_{10}$ is the 10-m wind vector, $\mathbf{U}_c$ is the current at $L/4\pi$ depth (where $L$ is the wavelength) from the ocean model, $\boldsymbol{\tau}_{\text{air}}$ is the momentum flux from the air (wind stress), $\boldsymbol{\tau}_c$ is the momentum flux into currents, $\psi_{\text{peak}}(k,\theta)$ is the wave spectrum around the peak, $\psi(k,\theta)$ is the full wave spectrum, and $f_{pi}$ is the input peak frequency.

The goal of this paper is to investigate the effects of wind–wave–current interaction on the ocean response to TCs using a coupled wind–wave–ocean model that includes explicit calculations of the wave boundary layer and the near-surface momentum flux budget. In particular, we seek to determine the effect of wind–wave–ocean coupling on the momentum fluxes into the ocean and wave models and the resulting ocean current and wave simulations. The outline of this paper is as follows. The wind–wave–ocean model and methodology of flux calculation are described in section 2. The experimental design is presented in section 3, and the results are discussed in section 4. Finally, a summary and conclusions are presented in section 5.

## 2. The coupled wind–wave–ocean model

A schematic diagram of the coupled wind–wave–ocean model developed in this study is shown in Fig. 1. The model includes three key processes that affect the air–sea momentum flux: sea state dependence, air–sea momentum flux budget, and wave–current interaction. Below we describe the components of the coupled model and the physics of their interaction.

### *a. Tropical cyclone wind model*

In this study, we use a simple TC wind field model, based on the analytical framework proposed by Holland

(1980). The model requires the central and ambient pressure, the maximum wind speed (MWS), and the radius of maximum wind speed (RMW) as inputs; it outputs wind speed as a function of radial distance from the center. In this study, the central and ambient pressure are set to be 968 hPa and 1012 hPa, respectively; the MWS is set to be 45 m $s^{-1}$; and the RMW is set to be 70 km. Real TCs are usually asymmetric in shape, with higher wind speed typically to the right of the TC track. The asymmetry of the wind field in our experiments is created by adding half of the translation speed (5 m $s^{-1}$ in this study) to the symmetric wind field, following Price (1981).

### b. Ocean model

The ocean response is calculated using the Princeton Ocean Model (POM). In brief, POM is a three-dimensional model structured on the primitive hydrodynamic equations with complete thermohaline dynamics (Blumberg and Mellor 1987). This model is fully nonlinear and incorporates the Mellor and Yamada level-2.5 turbulence closure scheme (MY scheme) (Mellor and Yamada 1982). After coupling POM with the GFDL hurricane model, Bender and Ginis (2000) have shown that the MY scheme produces good SST comparison with observations under hurricane conditions. They have also shown through real case studies that the coupled model significantly improves intensity prediction for Hurricanes Felix, Fran, Opal, and Gilbert. The GFDL hurricane–ocean coupled model was also tested on 163 cases during the 1995–98 hurricane seasons with significantly improved intensity forecasts obtained, particularly for the central pressure, which showed reductions in forecast errors of 26% (Ginis et al. 1999). Based on these results, the GFDL hurricane–ocean coupled model became operational in 2001. After comparing model results using five different mixing schemes with observations, Jacob et al. (2005) also concluded that the *K* profile parameterization (KPP) (Large et al. 1994) and MY schemes compare best to observations, followed closely by the Goddard Institute for Space Studies (GISS) scheme (Canuto et al. 2001). The HWRF operational hurricane coupled model also utilizes POM as its ocean module. In this study, the horizontal model domain of POM is set to be 30° latitude by 18° longitude with a grid increment of $^1/_{12}$° in both directions. The Coriolis parameter is set to be a constant and equal to $3.76 \times 10^{-5}$. The water depth is set to 2000 m for the whole model domain with 38 levels in the vertical. A vertical resolution of 10 m is used for the top 150 m. The ocean is assumed to be initially at rest and horizontally uniform. The initial vertical structure is defined using the climatological temperature profile in the Gulf of Mexico (25°N, 90°W) for the month of September, as shown in Fig. 2.

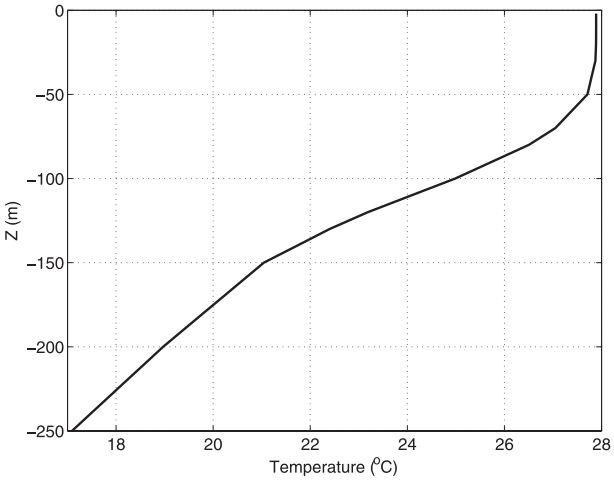


FIG. 2. Initial vertical temperature profile for the top 250 m at every grid point in POM.

### c. Wave model

We use the WWIII surface wave model developed and used operationally at NCEP (Tolman 2002). It explicitly accounts for wind input, wave–wave interaction, and dissipation due to white-capping and wave–bottom interaction and solves the spectral action density balance equation for directional wavenumber spectra. The wave spectrum of the model is discretized using 24 directions and 40 intrinsic (relative) frequencies extending from 0.0285 to 1.1726 Hz, with a logarithmic increment of $f_{n+1} = 1.1f_n$, where $f_n$ is the $n$th frequency. The intrinsic frequency is related to the wavenumber (magnitude) $k$ through the dispersion relation. In our experiments, the wave model domain is also set to 30° latitude by 18° longitude with a grid increment of $^1/_{12}$° in both directions. The water depth is set to be 2000 m for the whole model domain so that surface gravity waves have no interaction with the bottom. The standard output of the model also includes the significant wave height, the mean wavelength, and the input peak frequency $f_{pi}$, which corresponds to the peak of the wind-forced part of the wave spectrum.

### d. Air–sea interface model

The air–sea interface model consists of the wave boundary layer model (WBLM) and the air–sea momentum flux budget model (Fig. 1). The WBLM is described in detail in Moon et al. (2004a) and is used to estimate the momentum flux from air, or wind stress ($\boldsymbol{\tau}_{\text{air}}$), that depends on the sea state. First, the complete wave spectrum $\psi(k, \theta)$ is constructed by merging the WWIII spectrum $\psi_{\text{peak}}(k, \theta)$ in the vicinity of the

spectral peak with the spectral tail parameterization $\psi_{\text{tail}}(k,\theta)$ based on the equilibrium spectrum model of Hara and Belcher (2002). Here $k$ is the wavenumber and $\theta$ is the wave direction. Next, the wind profile and the wind stress profile are calculated based on the momentum and energy conservation across the wave boundary layer (Hara and Belcher 2004). Since the model treats the wind stress as a vector quantity to consider the influence of dominant waves that propagate at a large angle to the local wind, it allows us to estimate the wind stress $\boldsymbol{\tau}_{\text{air}}$ for any given surface wave field, even for complex seas encountered under TCs. In practice, the misalignment between the mean wind vector and the mean stress vector is at most a few degrees under TCs (Moon et al. 2004b).

In our coupled model, the ocean current has two ways of affecting the momentum flux and wave field. One way is through changing the 10-m wind velocity ($\mathbf{U}_{10}$) input to the WBLM by subtracting the current velocity $\mathbf{U}_c$ from $\mathbf{U}_{10}$ so that its magnitude and direction will change with the current. Consequently, the wind stress is modified. Another way is through the wave action equation in the WWIII:

$$\frac{\partial N}{\partial t} + \nabla x \cdot [(\mathbf{c}_g + \mathbf{U}_c)N] + \frac{\partial}{\partial k}(\dot{k}N) + \frac{\partial}{\partial \theta}(\dot{\theta}N) = \text{forcing}, \tag{1}$$

$$\dot{k} = -\mathbf{k} \cdot \frac{\partial \mathbf{U}_c}{\partial s},$$

$$\dot{\theta} = \frac{1}{k}\mathbf{k} \cdot \frac{\partial \mathbf{U}_c}{\partial m},$$

where $N = \psi/\omega$ is the wave action spectrum, $\omega$ is the relative (intrinsic) angular frequency ($\omega = 2\pi f$), $\mathbf{c}_g$ is the group velocity, $\mathbf{k}$ is the wavenumber vector, $s$ is a coordinate in the wave direction, $m$ is a coordinate perpendicular to $s$, and $\mathbf{U}_c$ is the ocean current at depth of $L/4\pi$ ($L$ is the mean wavelength calculated in WWIII). Refer to the appendix for explanation of why the current at depth $L/4\pi$ is used for the WWIII input. The variable ocean current not only modifies the speed of the wave action flux [second term of Eq. (1)] but also modifies the wavenumber of a particular wave packet as it propagates [third and fourth terms of Eq. (1)].

In the air–sea momentum flux budget model, the differences between the momentum flux from air ($\boldsymbol{\tau}_{\text{air}}$) and that into subsurface currents ($\boldsymbol{\tau}_c$) are estimated by explicitly calculating the momentum flux gained (or lost) by surface waves. The total momentum and the momentum flux in the wave field are first calculated from the complete wave spectrum obtained in WBLM. Then, the horizontal divergence of the horizontal momentum flux and the local time derivative of total momentum in the waves are calculated and subtracted from (or added to) the air input, $\boldsymbol{\tau}_{\text{air}} = (\tau_{\text{air\_}x}, \tau_{\text{air\_}y})$, to obtain $\boldsymbol{\tau}_c = (\tau_{c\_x}, \tau_{c\_y})$.

The horizontal momentum in $x$ and $y$ directions ($M_x$ and $M_y$) contained in the wave field are obtained from the complete wave spectrum as

$$M_x = \iint \rho_w \omega \psi(\omega,\theta) \cos\theta d\theta d\omega, \tag{2}$$

$$M_y = \iint \rho_w \omega \psi(\omega,\theta) \sin\theta d\theta d\omega. \tag{3}$$

The horizontal fluxes of $M_x$ and $M_y$ are obtained as

$$MF_{xx} = \iint \rho_w \omega C_g \psi(\omega,\theta) \cos^2\theta d\theta d\omega, \tag{4}$$

$$MF_{xy} = \iint \rho_w \omega C_g \psi(\omega,\theta) \cos\theta \sin\theta d\theta d\omega, \tag{5}$$

$$MF_{yy} = \iint \rho_w \omega C_g \psi(\omega,\theta) \sin^2\theta d\theta d\omega, \tag{6}$$

$$MF_{yx} = \iint \rho_w \omega C_g \psi(\omega,\theta) \sin\theta \cos\theta d\theta d\omega, \tag{7}$$

where $MF_{xx}$ is the horizontal flux of $M_x$ in the $x$ direction, $MF_{xy}$ is the horizontal flux of $M_x$ in the $y$ direction, $MF_{yy}$ is the horizontal flux of $M_y$ in the $y$ direction, and $MF_{yx}$ is the horizontal flux of $M_y$ in the $x$ direction. Then, the momentum flux $\boldsymbol{\tau}_c$ into subsurface currents is calculated as

$$\tau_{c\_x} = \tau_{\text{air\_}x} - \left(\frac{\partial MF_{xx}}{\partial x} + \frac{\partial MF_{xy}}{\partial y}\right) - \frac{\partial M_x}{\partial t}, \tag{8}$$

$$\tau_{c\_y} = \tau_{\text{air\_}y} - \left(\frac{\partial MF_{yx}}{\partial x} + \frac{\partial MF_{yy}}{\partial y}\right) - \frac{\partial M_y}{\partial t}. \tag{9}$$

On the right-hand side in Eqs. (8) and (9), the first term stands for the momentum flux input from air (wind stress), the second term in parentheses is the horizontal divergence of horizontal momentum flux, and the third term is the local time derivative of momentum in waves—that is, the momentum gained (lost) by growing (decaying) waves. This model was used by FanA and FanB to examine the air–sea momentum flux budget under growing seas and under TCs.

## 3. The experimental design

All numerical experiments in this paper are summarized in Table 1 and the corresponding diagrams for each experimental design are shown in Figs. 1 and 3. For simplicity, we assume that a TC is moving northward with constant translation speed 5 m $s^{-1}$ in all experiments. In the control experiment, the momentum flux

TABLE 1. Experimental designs. Here, $\mathbf{U}_c$ stands for current output from POM, $\boldsymbol{\tau}_{\text{air}}$ stands for momentum flux from the air, and $\boldsymbol{\tau}_c$ stands for the momentum flux into currents.

| Expt | Current input to wave model | Current input to wave boundary layer model | Ocean model forcing |
|---|---|---|---|
| Control | 0 | 0 | $\boldsymbol{\tau}_{\text{air}}$ |
| A | 0 | 0 | $\boldsymbol{\tau}_c$ |
| B | $\mathbf{U}_c$ | $\mathbf{U}_c$ | $\boldsymbol{\tau}_{\text{air}}$ |
| C | 0 | $\mathbf{U}_c$ | $\boldsymbol{\tau}_{\text{air}}$ |
| D | $\mathbf{U}_c$ | $\mathbf{U}_c$ | $\boldsymbol{\tau}_c$ |

from the air $\boldsymbol{\tau}_{\text{air}}$ is calculated by the WBLM at every time step and then used to force the WWIII and POM. There is no feedback from POM to WBLM in this experiment; therefore, it represents a one-way interaction between the atmosphere and ocean. In experiment A, the air–sea momentum flux budget calculation is included as described by Eqs. (8) and (9) in which the net momentum flux gain in the wave field is subtracted from $\boldsymbol{\tau}_{\text{air}}$ and the remaining momentum flux $\boldsymbol{\tau}_c$ is used to force POM. Since there is no feedback from the ocean to atmosphere in this experiment, it also represents a one-way interaction. In experiment B, a two-way interaction is introduced by including the ocean current effects. There are two ways that the ocean current $\mathbf{U}_c$ impacts the momentum flux and wave field: 1) in the calculation of $\boldsymbol{\tau}_{\text{air}}$ in the WBLM (i.e., the effective wind forcing becomes $\mathbf{U}_{10} - \mathbf{U}_c$ rather than $\mathbf{U}_{10}$) and 2)in the wave action equation (1) that is solved in WWIII. Both effects are included in experiment B. The air–sea momentum flux budget calculation is excluded in this experiment; that is, $\tau_{\text{air}}$ is used to force POM. Experiment C is designed to determine which current effect is more important; it is the same as experiment B except that the effect of current in the wave action equation (in WWIII) is not considered. Finally, all the above effects are considered in experiment D through a complete wind–wave–current interaction by using $\boldsymbol{\tau}_c$ to force POM and the feedback of $\mathbf{U}_c$ to WBLM and WWIII at every time step.

## 4. Results and discussion

### a. Control experiment

The wind stress in the control experiment (see diagram in Fig. 3) at 84 h is shown in Fig. 4a. It is rightward biased relative to the TC track owing to the imposed asymmetry in the wind field. The asymmetry in the momentum flux is further enhanced by the hurricane-induced waves (Fig. 5a). The waves in the right front

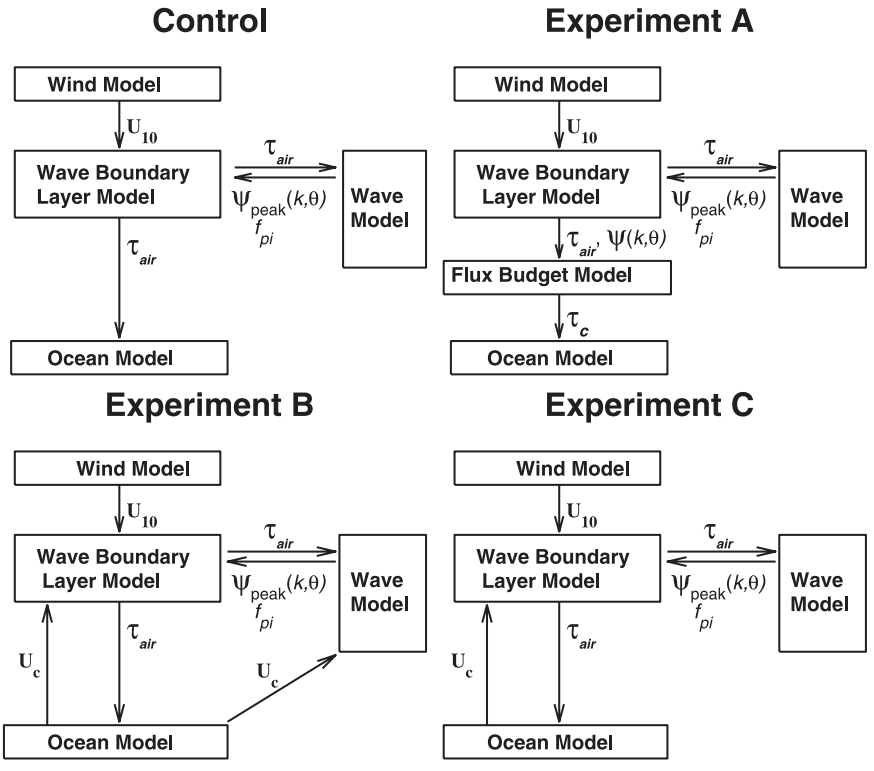


FIG. 3. Experimental design for the control experiment and experiments A–C. The experimental design for experiment D is given in Fig. 1. The variables in this figure are the same as described in Fig. 1.

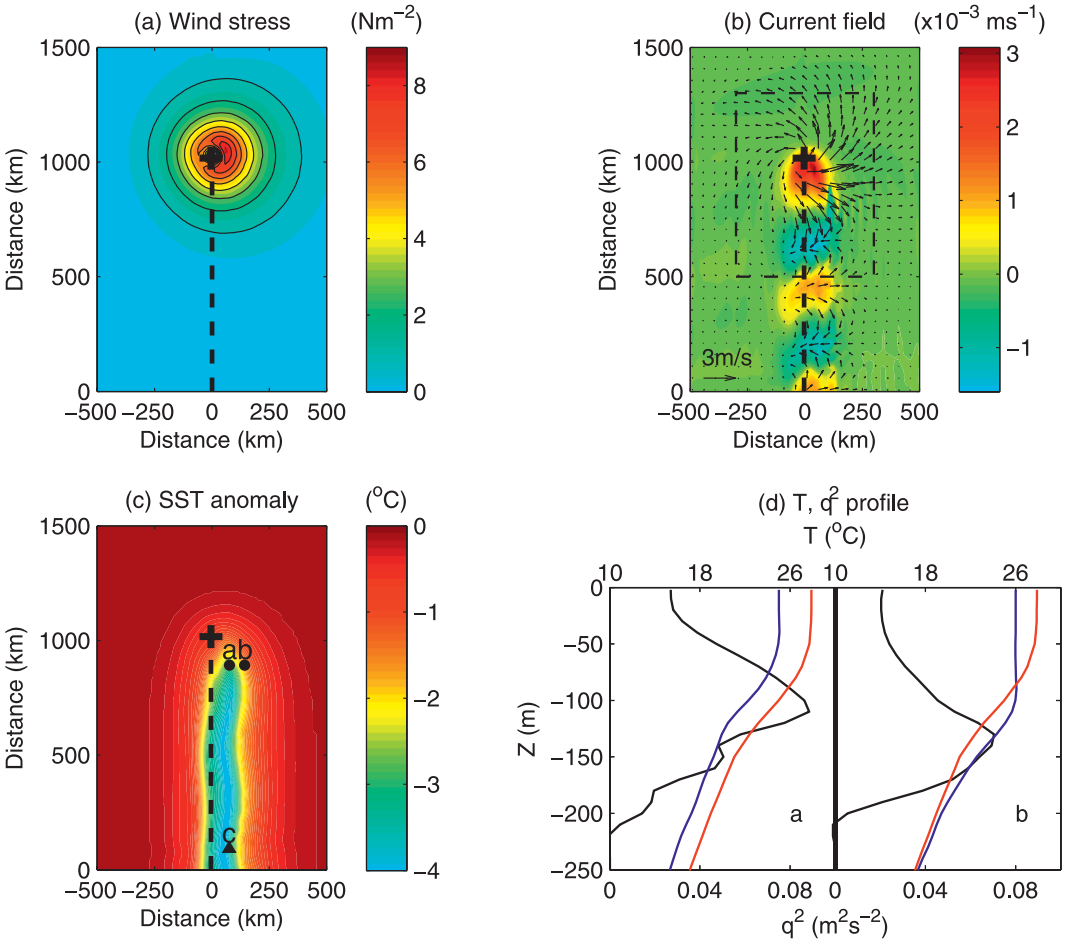


FIG. 4. The control experiment after 84 h of calculation: (a) air input momentum flux (wind stress), with contours at every 1 N m$^{-2}$; (b) surface horizontal currents (vectors) and upwelling velocity $w$ at 90-m depth (color scale; positive value indicates upward motion); (c) sea surface temperature anomaly from that at the initial time; and (d) turbulent kinetic energy ($q^2$; black), temperature (blue), and the initial ocean temperature (red) profile at the location indicated by dots a and b in (c). The black cross and dashed line in (a)–(c) indicate the center and track of the TC.

quadrant of the storm track are higher and longer due to the resonance effect caused by the movement of the hurricane (Moon et al. 2004b), while those in the left rear quadrant are lower and shorter. The wave field pattern is in good agreement with observations and other modeling studies (Wright et al. 2001; Moon et al. 2003).

Figure 4b shows the currents in the upper ocean in the control experiment. The structure of the internal near-inertial frequency wave wake is represented by alternating cells of upwelling and downwelling, as indicated by the vertical velocity contours in Fig. 4b. The rightward bias in the surface current field is a characteristic feature of the ocean response to a moving storm and is well known from previous observational and numerical studies (Price 1981; Ginis 2002). The rightward bias in the sea surface temperature cooling shown in Fig. 4c is a result of the rightward bias in the hurricane-induced turbulent mixing in the water column. The maximum cooling in the cold wake is near 3.7°C and located at 1–2 radii of the maximum winds ($R_{max}$) behind the storm center. This is also in good agreement with previous studies (Price 1981). Temperature and TKE profiles are shown in Fig. 4d at locations **a** and **b** (indicated by the dots in Fig. 4c) of $R_{max}$ and $2R_{max}$ to the right of the storm track. They show strong upwelling (a temperature decrease throughout the entire water column) at $R_{max}$ and weak downwelling at $2R_{max}$. The mixed layer depth is increased to about 120 m at $2R_{max}$ due to both intense turbulent mixing and downward motion. The TKE profile has its maximum underneath the mixed layer where the vertical velocity shear is the largest.

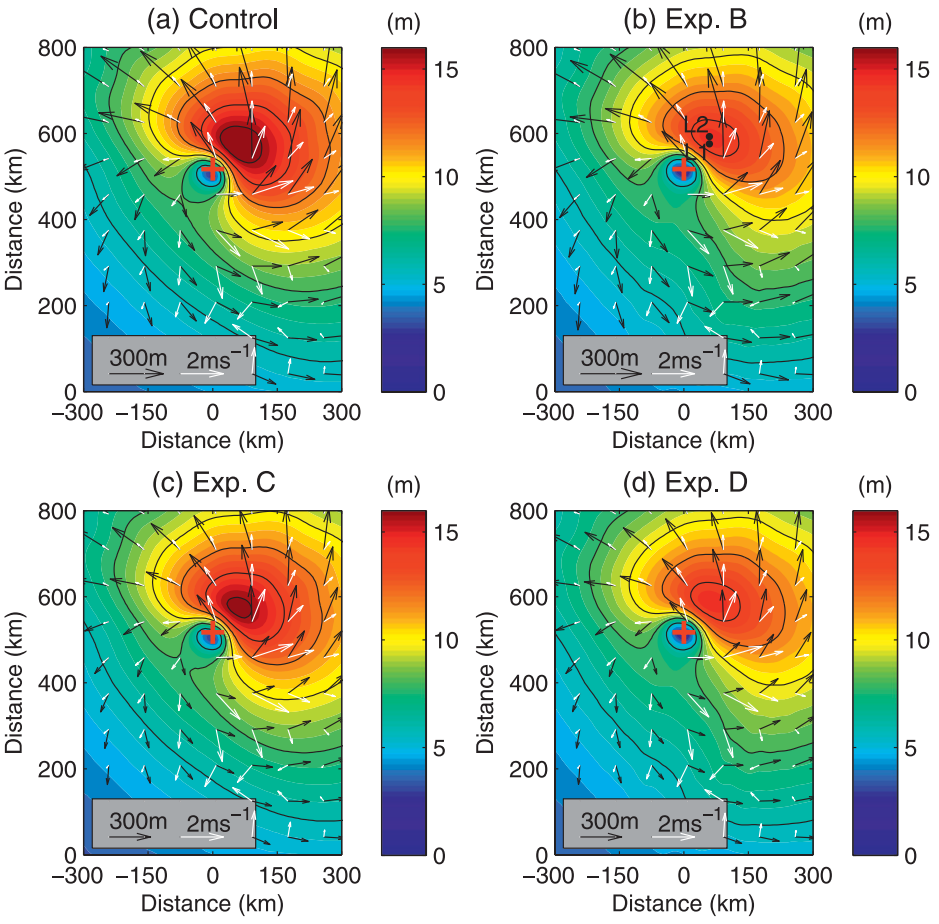


FIG. 5. Surface gravity wave field for (a) the control and (b)–(d) experiments B, C, and D, respectively. Colors and contours are significant wave height in meters; the contours are given at 2-m intervals; black arrow length indicates mean wavelength and direction indicates mean wave direction; white arrows represent ocean currents. The red cross indicates the center of the TC.

This causes the entrainment of cold thermocline water into the mixed layer and the reduction of SST.

The ocean response in this and other experiments typically reaches a quasi-steady state relative to the TC center after about 78 h of model integration. In the following sections, we will therefore analyze the model fields at $t = 84$ h in the rectangular region with black dashed boundaries shown in Fig. 4b.

### b. *Effect of air–sea momentum flux budget on the momentum flux and ocean response*

The effect of the air–sea momentum flux budget on the momentum flux into the subsurface currents is shown in Fig. 6a (experiment A), where $\boldsymbol{\tau}_c$ is calculated using Eqs. (8) and (9). It is seen that the ratio of $|\boldsymbol{\tau}_c|$ and $|\boldsymbol{\tau}_{\text{air}}|$ is reduced by 6% in the right rear quadrant of the TC. There is also a small clockwise rotation by a few degrees between $\boldsymbol{\tau}_c$ and $\boldsymbol{\tau}_{\text{air}}$. The impact of the reduced momentum flux into the ocean on the surface currents is presented in Fig. 7a, which shows the current vector difference between experiment A and the control experiment as well as its magnitude (in color). The effect of the reduced flux on the current direction is negligibly small, but the current speed is reduced by up to 0.11 m s$^{-1}$, mostly on the right side of the TC track. As shown in Fig. 8, the spatially averaged TKE profile (calculated in the black dashed box in Fig. 4b) in experiment A (black solid line) reaches its maximum at the same depth as the TKE profile in the control experiment, but with smaller magnitude. With less turbulent mixing in the upper ocean, the SST in the cold wake is increased by up to 0.3°C, which corresponds to about a 10% reduction of the SST cooling compared with the control experiment (Fig. 9a). Also, notice an area with enhanced $\boldsymbol{\tau}_c$ in the upper right corner of Fig. 6a. This is because large waves propagate into smaller waves in this region and give up momentum to the subsurface currents (FanA; FanB).

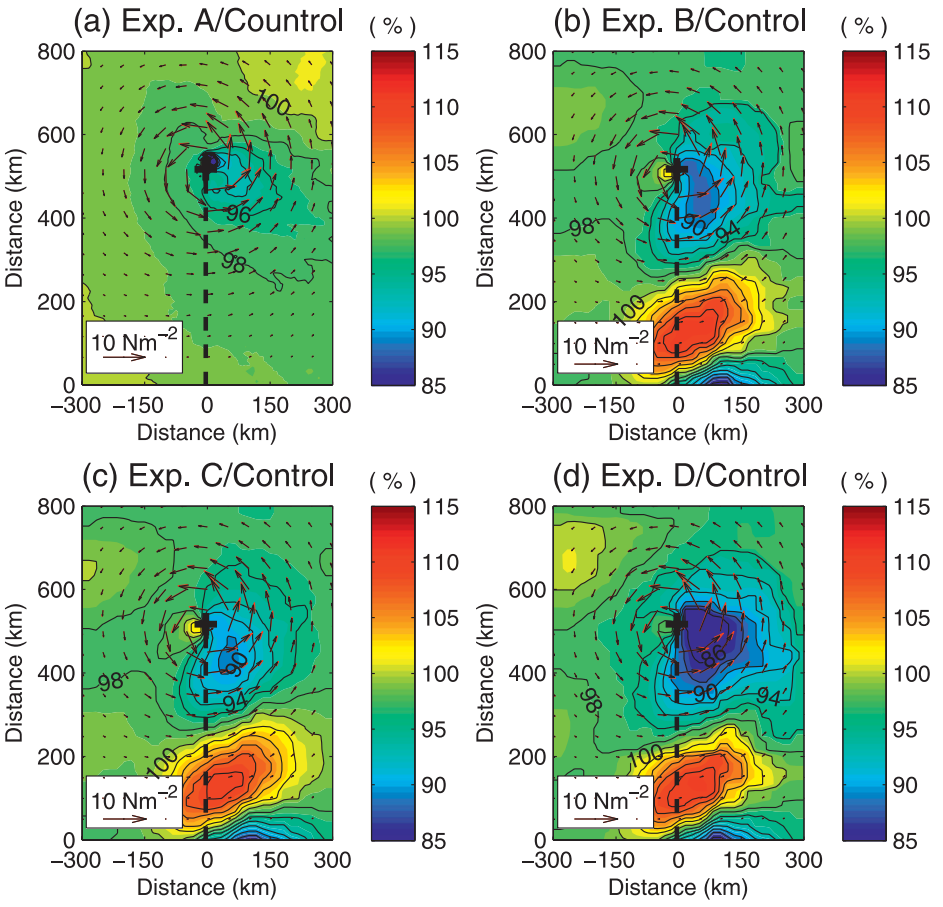


FIG. 6. Percentage of momentum flux into the ocean model ($\boldsymbol{\tau}_c$) in experiments (a) A, (b) B, (c) C, and (d) D relative to the wind stress ($\boldsymbol{\tau}_{\text{air}}$) in the control case at every 2% interval. Red arrows show $\boldsymbol{\tau}_{\text{air}}$ in the control experiment and black arrows show $\boldsymbol{\tau}_c$ in the corresponding experiments from A to D. The black cross and dashed line indicate the center and track of the TC.

### c. *Effect of wind–wave–current interaction on the ocean response*

In experiment B (see diagram in Fig. 3), the effect of wind–wave–current interaction is considered. However, the air–sea momentum flux budget is not considered; that is, the ocean model is forced directly by the wind stress. The ratio between the wind stresses in experiment B and the control experiment is presented in Fig. 6b. The magnitude of the wind stress is reduced by up to 10% in the right rear quadrant of the TC where the surface current is the strongest (Fig. 4b). Interestingly, there is an area at ~300 km behind the TC where the wind stress in experiment B is larger than that in the control experiment. This is because the current and wind vectors have opposite directions. But, since this area is far away from the TC center where the winds are weak, the increase of wind stress does not affect the ocean response appreciably. The reduced wind stress in experiment B causes a reduction of the surface current speed up to 0.2 m s$^{-1}$ to the right of the storm track (Fig. 7b) compared to the control experiment. As a result, the turbulent mixing in the upper ocean is reduced (Fig. 8) and the SST in the cold wake is increased by up to 0.5°C (Fig. 9b) relative to the control experiment.

Experiment C is as in experiment B except the ocean current $\mathbf{U}_c$ is neglected in the wave action equation (1). The ratio between the wind stresses in this experiment and the control experiment is shown in Fig. 6c. It is evident that this figure and Fig. 6b are almost identical—the percentage differs by less than 1% everywhere between the two figures. This indicates that the reduction of the wind stress seen in experiment B is primarily due to the subtraction of $\mathbf{U}_c$ from $\mathbf{U}_{10}$ in the WBLM rather than to the effect of ocean currents on the wave actions. As the wind stresses in experiments C and B are

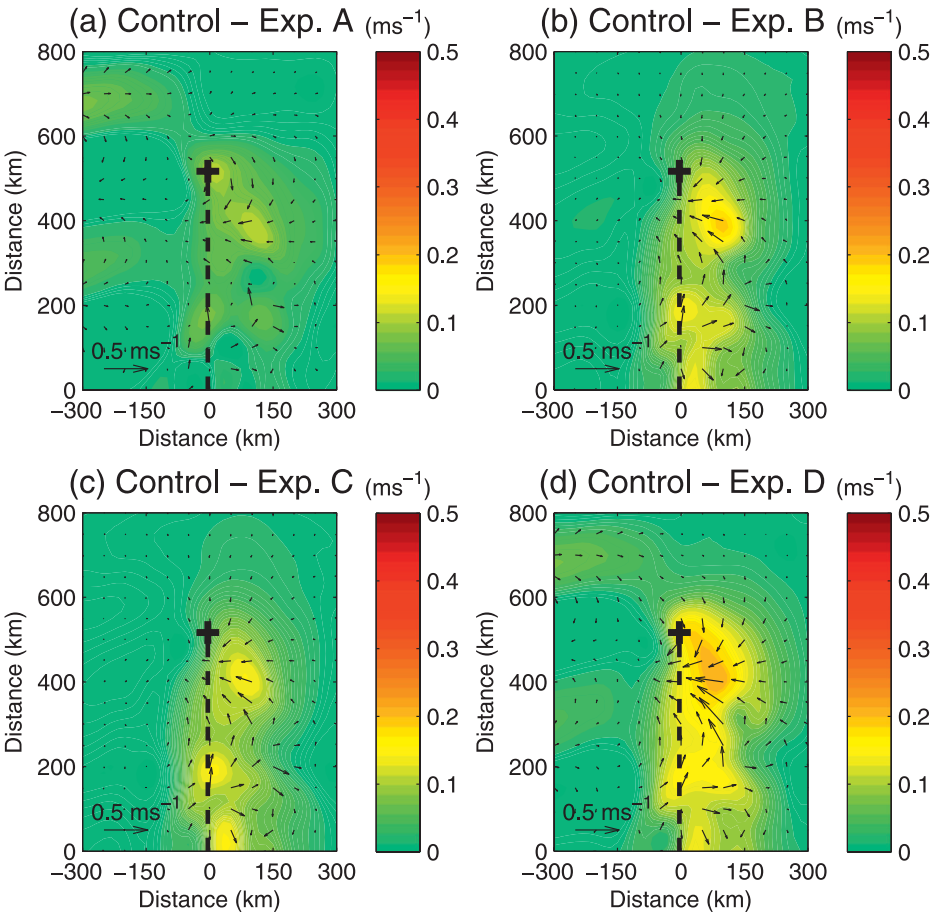


FIG. 7. Surface current differences between experiments (a) A, (b) B, (c) C, and (d) D and the control case, respectively. Arrows show the vector difference and color scale indicates the difference in magnitude. The black cross and dashed line indicate the center and track of the TC.

almost the same, so are the TC-generated surface currents (Figs. 7c), TKE profiles (Fig. 8), and SST cooling (Figs. 9c).

### *d. Effect of wind–wave–current interaction on the wave field*

Next, we consider the TC-generated surface waves in each experiment. Comparing the wave fields in the control experiment (Fig. 5a) and experiment B (Fig. 5b), we notice that the significant wave height $H_s$ in experiment B is significantly reduced in the right front quadrant of the TC owing to the impact of surface currents. Figure 10 shows the locations of $H_s$ maxima relative to the storm center in all experiments. In experiment B, the location of the $H_s$ maximum (L2) is shifted by about 15 km in the direction of the storm motion from its location in the control experiment (L1). The directional wavenumber spectra at locations L1 and L2 are shown in Fig. 11 and the frequency spectra in Fig. 12. The significant wave height is lower and the

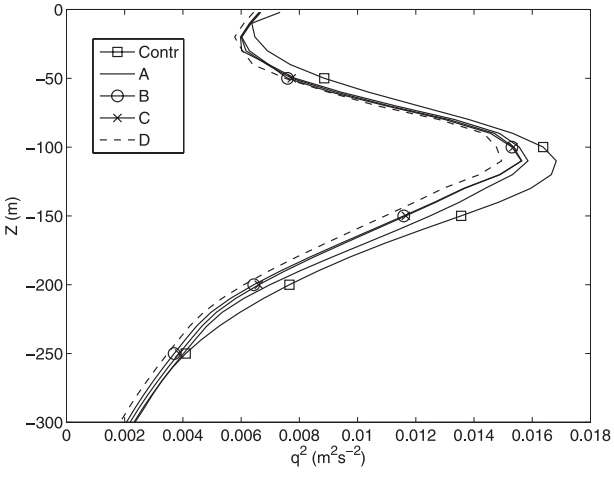


FIG. 8. Spatially averaged turbulent kinetic energy ($q^2$) in the box shown in Fig. 4b for experiments A, B, C, and D compared with the control experiment.

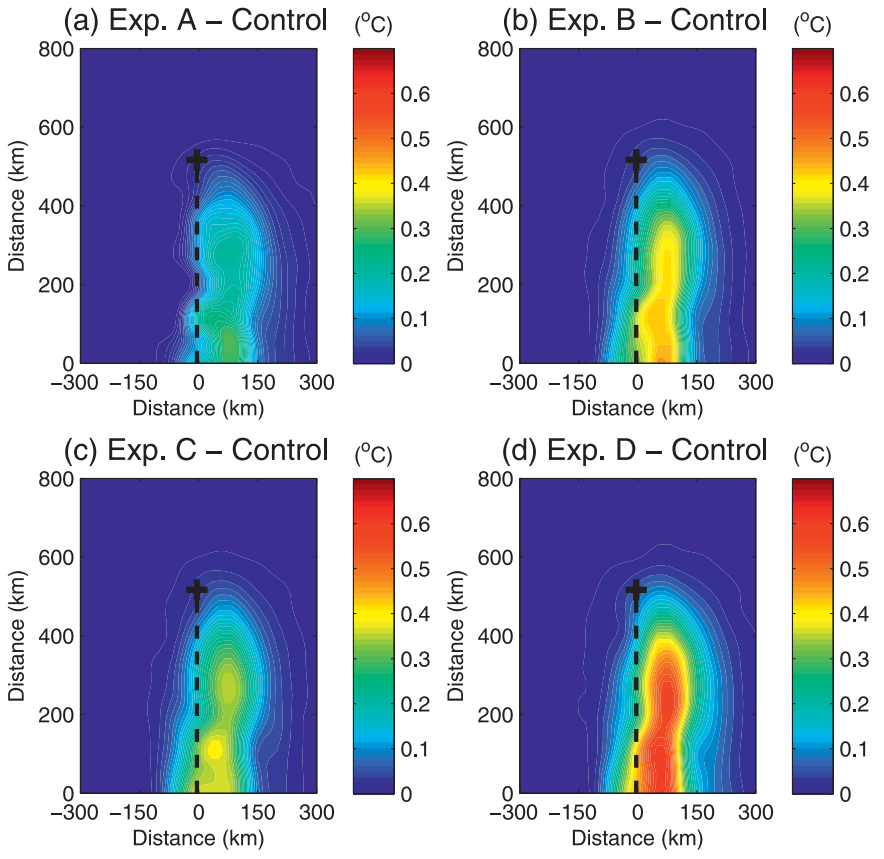


FIG. 9. SST anomaly differences between experiments (a) A, (b) B, (c) C, and (d) D and the control case. The color scale represents temperature in degrees (°C); positive (negative) denotes decrease (increase) of SST cooling. The black cross and dashed line indicate the center and track of the TC.

dominant wavelength is shorter at both locations when the current effect is included. The maximum significant wave height is reduced from 17.0 to 14.7 m and the dominant wavelength is reduced from 359 to 319 m. Another important effect of the wave–current interaction is a reduction of the frequency spectra and a shift of the spectral peak to higher frequencies (Fig. 12).

To interpret the above results we examine the wave–current interaction using the wave action equation (1). As the direction of the ocean current at locations L1 and L2 is almost the same as the direction of the storm motion and the direction of the dominant waves is about 15° to the left (Fig. 11), we can consider for simplicity a one-dimensional approximation of Eq. (1). We can also neglect the time tendency term because both the current and wave fields are in quasi-steady state relative to the storm. Equation (1) in a storm-following coordinate then becomes

$$\frac{\partial N}{\partial s}(U_c + C_g - U_t) - k\frac{\partial N}{\partial k}\frac{\partial U_c}{\partial s} = \text{forcing}, \qquad (10)$$

where $U_t$ is the hurricane translation speed ($U_t = 5$ m s$^{-1}$ in our experiment) and $s$ is a coordinate measured from the location of interest (L1 or L2) in the direction of current and waves. When waves are compressed or stretched by a spatially varying current, the resulting modulation of the wave action is expressed by the term

$$k\frac{\partial N}{\partial k}\frac{\partial U_c}{\partial s}.$$

This is mostly balanced by the first (advection of wave action) term

$$\frac{\partial N}{\partial s}(U_c + C_g - U_t)$$

for lower frequencies because the forcing term is relatively small. Notice that the current is largest around locations L1 and L2 (Fig. 5b); hence, $\partial U_c/\partial s > 0$ for $s < 0$ and $\partial U_c/\partial s < 0$ for $s > 0$. Since $k\partial N/\partial k$ is always negative, we have

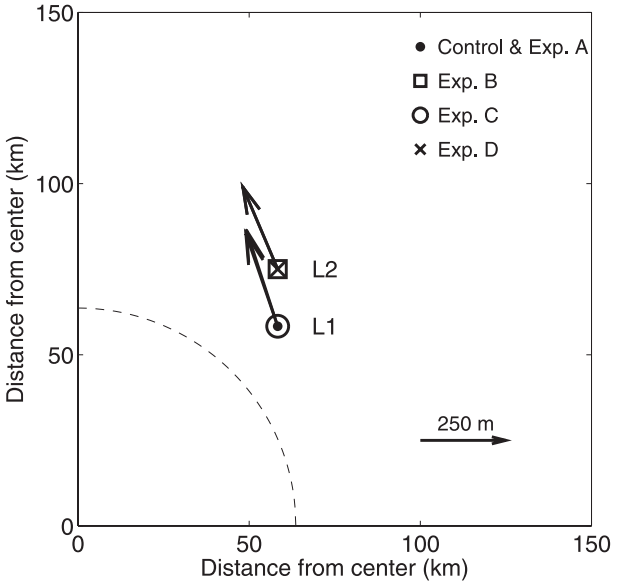


FIG. 10. The location of maximum significant wave height relative to the center of the TC at hour 84 of model calculation, and the wavelength (arrow length) and propagation direction (arrow pointing direction) at that location. The dashed line shows the radius of maximum wind.

$$\begin{cases} k\dfrac{\partial N}{\partial k}\dfrac{\partial U_c}{\partial s} < 0; & \dfrac{\partial N}{\partial s}(U_c + C_g - U_t) < 0,\ s < 0 \\ k\dfrac{\partial N}{\partial k}\dfrac{\partial U_c}{\partial s} > 0; & \dfrac{\partial N}{\partial s}(U_c + C_g - U_t) > 0,\ s > 0. \end{cases} \tag{11}$$

Then, the sign of $\partial N/\partial s$ is determined by the sign of $U_c + C_g - U_t$, that is, depending on whether the wave packet propagates faster or slower than the TC. When $U_c = 2\ \mathrm{m\ s^{-1}}$, $U_c + C_g - U_t$ is always positive for lower frequencies, and the spectra in the maximum current region are reduced. However, as the wave frequency increases, the forcing term in (10) becomes increasingly important and the modulation of the spectrum is reduced. Such a trend is indeed observed in Fig. 12. Also notice that because of the horizontal current shear, the angular distribution of the wave energy is widened. This result is consistent with the Tolman et al. (1996) study of wave interference with the Gulf Stream.

When the ocean current is neglected in the wave action equation in experiment C, we find that the resulting wave fields are quite different from those in experiment B. The maximum significant wave height is reduced by only 0.7 m compared to the control case (Fig. 5c), and its locations and the dominant wave direction are virtually the same as the control case (Fig. 10). These results indicate that the modulation of the wave actions by the ocean current is primarily responsible for the differences in the wave fields between experiment B and the control experiment. We can also conclude that the reduction of the wind stress input to the WWIII due to the subtraction of $\mathbf{U}_c$ from $\mathbf{U}_{10}$ in the WBLM, which is included in experiment C, has a very small effect on the wave field.

### e. Full wind–wave–current coupling

In experiment D we apply the fully coupled wind–wave–ocean model (see the diagram in Fig. 1) including the air–sea flux budget calculation. The ratio between $|\boldsymbol{\tau}_c|$ in this experiment and $|\boldsymbol{\tau}_{\mathrm{air}}|$ in the control experiment is presented in Fig. 6d. Comparing this ratio with those in experiments A–C, we notice that the magnitude of the momentum flux into the ocean is further reduced to as low as 86% in the right rear quadrant of the TC, where the ocean current is the strongest and the spatial gradient in the wave field is the largest. There is some small rotation of $\boldsymbol{\tau}_c$ to the right of $\boldsymbol{\tau}_{\mathrm{air}}$ by a few degrees due to the spatial variation of the wave field. The reduction of the surface current in the TC wake is the largest (up to $0.25\ \mathrm{m\ s^{-1}}$, Fig. 7d) and the averaged TKE profile shows the smallest magnitude among all experiments (Fig. 8). The SST is increased by up to 0.65°C (Fig. 9d); that is, the SST cooling is reduced by approximately 20% compared to the control experiment (Fig. 4c).

Figures 13a and 13b show the vertical temperature profile time series in the upper 250 m at a location 70 km to the right of the track in the control experiments and experiment D. The mixed layer depth, shown by the black lines, is defined to be the lowest sigma level at which the difference between the SST and the temperature at that sigma level is less than 0.5°C. The temperature profiles show the cooling throughout the mixed layer after the passage of the storm center. Not only is the SST cooling reduced in experiment D, but the mixed layer depth also becomes shallower compared to the control experiment. Upwelling due to the Ekman divergence caused by the cyclonic winds (positive wind stress curl) and oscillations of the isotherms at a near-inertial period (the inertial period is 28.8 h for this study) are evident following the storm passage. Figure 13c shows the difference between the temperatures in experiment D and the control experiment. The warmer (colder) temperature anomalies in the thermocline indicate that the upwelling (downwelling) rates are less in experiment D compared to the control experiment. This clearly implies that the wind–wave–current interaction processes at the air–sea interface affect not only the upper mixed layer but also the thermocline below.

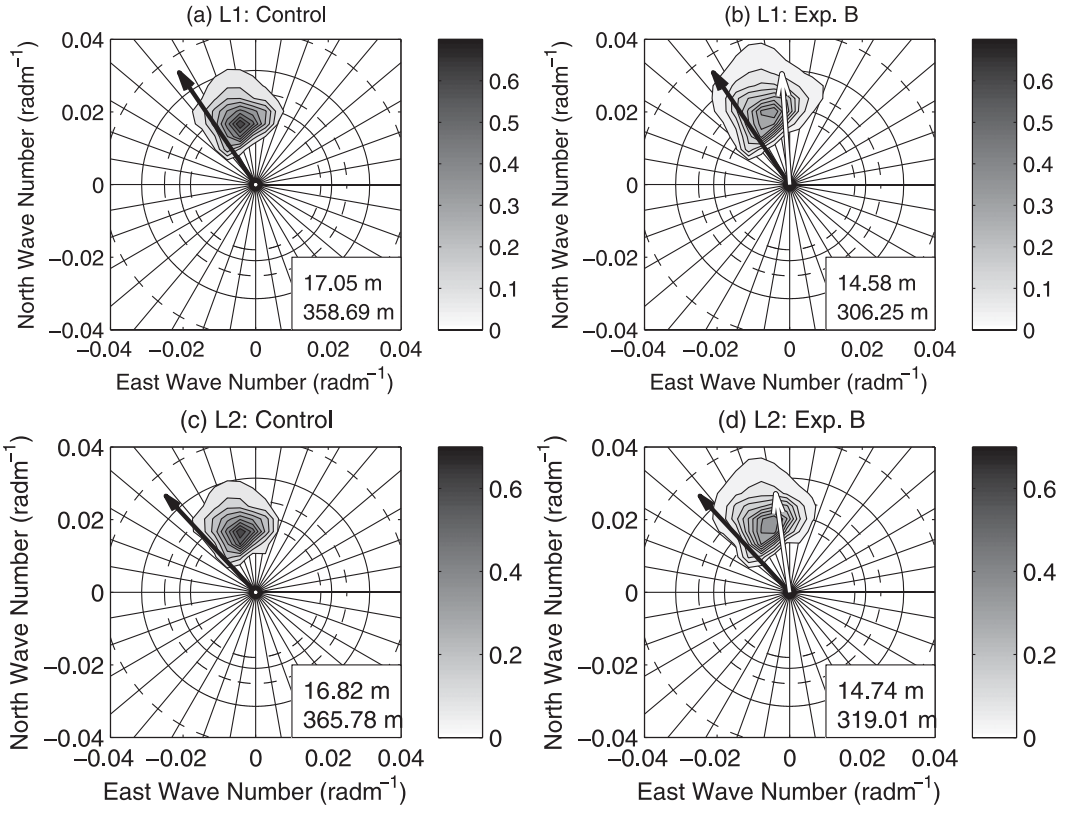


FIG. 11. WWIII spectra at location L1 for (a) the control and (b) experiment B and at location L2 for (c) the control and (d) experiment B. (The locations are shown in Fig. 5b.) The dashed circles (outer to inner) correspond to wavelengths of 150, 250, and 350 m. The solid circles indicate wavelengths of 200 and 300 m. Each spectrum contains nine contours, linearly spaced from 10% to 90% of the peak spectral density in m$^4$ rad$^{-2}$ (color bar). The significant wave height and dominant wavelength are shown with each spectrum. The black and white arrows represent the wind and current at that location.

## 5. Summary and conclusions

In this paper, we have investigated the wind–wave–current interaction processes at the air–sea interface in TCs. We have examined their effect on the momentum fluxes into the ocean and wave models and the resulting changes in the ocean and surface wave field responses. We developed a coupled wind–wave–ocean model that includes three key processes that affect the air–sea momentum flux: sea state dependence, momentum flux

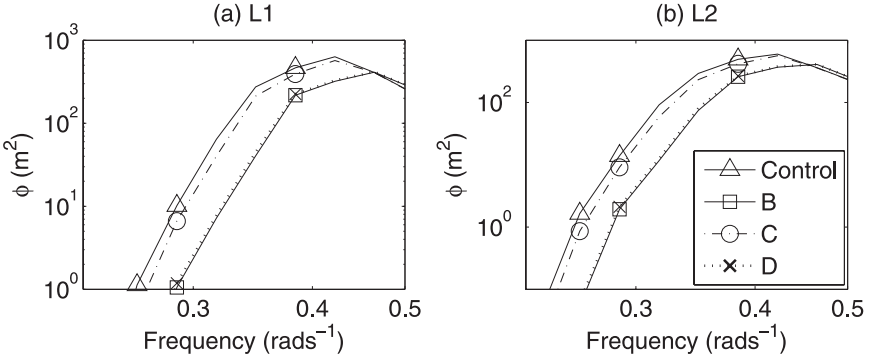


FIG. 12. Comparison of frequency spectra $\phi$ ($\phi = \int \psi d\theta$) for different experiments at locations (a) L1 and (b) L2. The locations are shown in Fig. 5b.

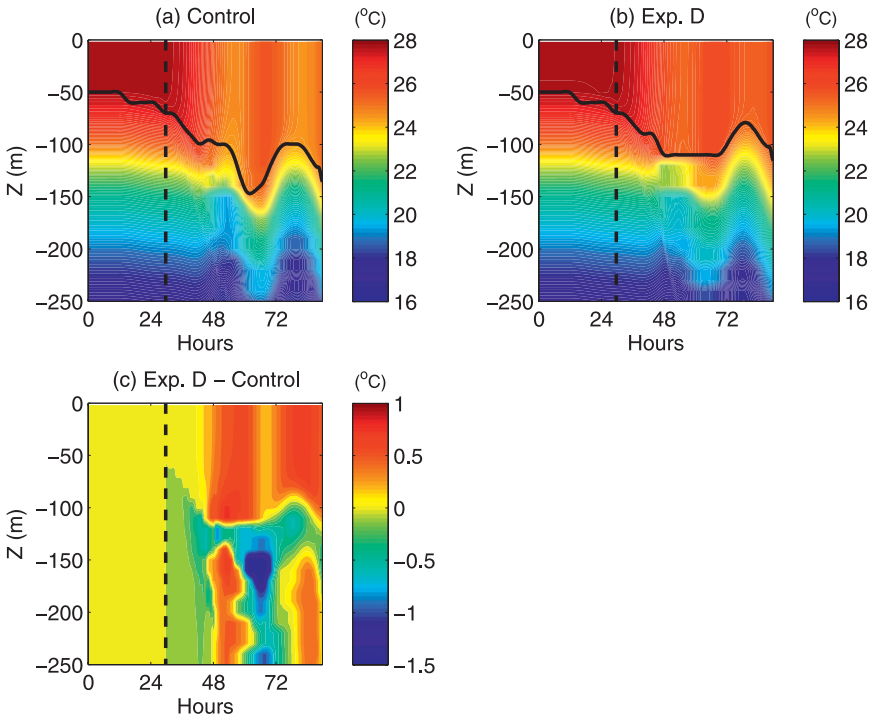


FIG. 13. (a),(b) Time series from the beginning of the model in integration of temperature profile at locations C (given in Fig. 4c) for the (a) control experiment and (b) experiment D. (c) The difference between experiment D and the control experiment. The black curve in (a) and (b) shows the mixed layer depth, and dashed line in all panels shows the time when the storm center passed the latitude of locations C.

budget at the air–sea interface, and wave–current interaction. The model consists of the WAVEWATCH III wave model, the Princeton Ocean Model, the wave boundary layer model by Moon et al. (2004a), and the air–sea momentum flux budget model.

A set of idealized numerical experiments was conducted in which a TC, represented by a simple surface wind model, moved over the ocean with constant speed. In the control experiment, the wave and ocean models were forced by the wind stress calculated in the wave boundary layer model. In experiment A, the effect of the air–sea momentum flux budget on the momentum flux into the subsurface currents was included. In experiments B and C, different feedback mechanisms of the ocean current on the wind stress and the wave field were analyzed. In experiment D, the effect of full wind–wave–current coupling was investigated.

We found that a growing surface wave field may take a significant fraction of the momentum flux from air. The momentum flux into subsurface currents was reduced compared to the wind stress by as much as 6% in experiment A. This effect was most significant in the right rear quadrant of the TC where the wave field had the largest spatial gradients. The reduction of the momentum flux into the ocean consequently reduced the magnitude of the subsurface current and sea surface temperature cooling to the right of the storm track. The SST in the cold wake was increased by up to 0.3°C; that is, the cooling was reduced by about 10% compared to the control experiment.

The inclusion of the wave–current interaction in experiment B also led to reduction of the momentum flux into the ocean in the right rear quadrant of the TC. This reduction was mainly due to subtraction of the surface current velocity from the wind speed when the wind and current vectors are closely aligned. In this experiment, the surface current was reduced by up to 0.2 m $s^{-1}$ and the maximum SST cooling in the cold wake was reduced by 0.5°C compared to the control experiment. In the fully coupled wind–wave–current experiment with the air–sea momentum flux budget calculation, the momentum flux into the ocean was reduced by up to 14% and the maximum SST cooling in the cold wake was reduced by 0.65°C, which is about 20% of the maximum cooling in the control experiment. The warmer (colder) temperature anomalies in the thermocline indicate that the upwelling (downwelling) rates are less in experiment D compared to the control experiment. The

wind–wave–current interaction processes therefore affected the rates of upwelling/downwelling in the thermocline after the storm passage.

We found that the wave field was also significantly affected by the wind–wave–current interaction. The maximum of the significant wave height was reduced in the right front quadrant of the TC from 17.0 to 14.7 m and the dominant wavelength was reduced from 359 to 319 m. The location of the maximum significant wave height was shifted by about 15 km in the direction of the storm motion. Another important effect of the wave–current interaction was a reduction of the frequency spectra at lower frequencies and a shift of the spectral peak to higher frequencies. From the analysis of the wave action equation we concluded that the wave field was mostly modulated by the horizontal gradient of the currents and the horizontal current advection of waves. The reduction in the momentum flux due to the differences between the wind and current velocities had a very small effect on the wave field response.

In summary, our numerical modeling study suggests that the wind–wave–current interaction processes in TCs may have significant effects on the wave and ocean responses. This may have important feedbacks on the TC track and intensity. For example, the reduction of the storm-induced SST cooling may lead to an increase of the TC intensity. We plan to investigate these feedbacks in our future modeling studies.

*Acknowledgments.* This work was supported by the U.S. National Science Foundation through Grant ATM 0406895. TH and IG also thank the U.S. Office of Naval Research (CBLAST program, Grant N00014-06-10729) for additional support.

## APPENDIX

### Depth for Considering the Current Effect on Gravity Waves

Let us consider a linear surface wave train in the presence of a surface current that is vertically sheared and is horizontally homogeneous. We start with the Euler equation that only varies in $x$ and $z$ directions ($\partial/\partial y = 0$):

$$\frac{\partial u}{\partial t} + u\frac{\partial u}{\partial x} + w\frac{\partial u}{\partial z} = -\frac{1}{\rho}\frac{\partial P}{\partial x}, \tag{A1}$$

$$\frac{\partial v}{\partial t} + u\frac{\partial v}{\partial x} + w\frac{\partial v}{\partial z} = 0, \tag{A2}$$

$$\frac{\partial w}{\partial t} + u\frac{\partial w}{\partial x} + w\frac{\partial w}{\partial z} = -\frac{1}{\rho}\frac{\partial P}{\partial z}, \tag{A3}$$

$$\frac{\partial u}{\partial x} + \frac{\partial w}{\partial z} = 0, \tag{A4}$$

where $P$ is the dynamic pressure. Now, separating the horizontal velocity into a depth-varying mean flow and a wave perturbation as $u = U(z) + u'$ and $v = V(z) + v'$ and substituting these into (A1)–(A4) and linearizing the equations, we obtain

$$\frac{\partial u'}{\partial t} + U\frac{\partial u'}{\partial x} + w\frac{\partial U}{\partial z} = -\frac{1}{\rho}\frac{\partial P}{\partial x}, \tag{A5}$$

$$\frac{\partial v'}{\partial t} + U\frac{\partial v'}{\partial x} + w\frac{\partial V}{\partial z} = 0, \tag{A6}$$

$$\frac{\partial w}{\partial t} + U\frac{\partial w}{\partial x} = -\frac{1}{\rho}\frac{\partial P}{\partial z}, \tag{A7}$$

$$\frac{\partial u'}{\partial x} + \frac{\partial w}{\partial z} = 0. \tag{A8}$$

The corresponding surface boundary conditions are

$$U\frac{\partial \varsigma}{\partial x} + \frac{\partial \varsigma}{\partial t} = w, \quad P - \rho g\zeta = 0 \text{ at } z = 0, \tag{A9}$$

where $\zeta$ is the surface displacement. Setting $(u', v', w, P, \varsigma) = (u_0, v_0, w_0, P_0, \varsigma_0)e^{ikx - i\sigma t}$ and substituting into (A9)–(A13), we get

$$-i\sigma u_0 + ikUu_0 + w_0\frac{\partial U}{\partial z} = -\frac{1}{\rho}ikP_0, \tag{A10}$$

$$-i\sigma v_0 + ikUv_0 + w_0\frac{\partial V}{\partial z} = 0, \tag{A11}$$

$$-i\sigma w_0 + ikUw_0 = -\frac{1}{\rho}\frac{\partial P_0}{\partial z}, \tag{A12}$$

$$iku_0 + \frac{\partial w_0}{\partial z} = 0, \tag{A13}$$

$$ikU\varsigma_0 - i\sigma\varsigma_0 = w_0, \quad P_0 = \rho g\varsigma_0 \text{ at } z = 0. \tag{A14}$$

Here $\sigma$ is the absolute angular frequency that is different from the relative (intrinsic) angular frequency $\omega$ in the presence of a current. Combining Eqs. (A10), (A12), and (A13), we get

$$\frac{\partial^2 w_0}{\partial z^2} + \left(\frac{\partial^2 U/\partial z^2}{\sigma/k - U} - k^2\right)w_0 = 0. \tag{A15}$$

If $U$ varies linearly with depth ($\partial U/\partial z = \text{const}$), then (A15) can be simplified to

$$\frac{\partial^2 w_0}{\partial z^2} - k^2 w_0 = 0, \tag{A16}$$

which gives $w_0 = e^{\pm kz}$. Since $w = 0$ when $z \to -\infty$, we have

$$w_0 = e^{kz}, \tag{A17}$$

so

$$u_0 = ie^{kz}, \quad P_0 = i\rho\left(\frac{\sigma}{k} - U + \frac{1}{k}\frac{\partial U}{\partial z}\right)e^{kz}. \tag{A18}$$

The boundary conditions yield

$$ik\left(U|_{z=0} - \frac{\sigma}{k}\right)\varsigma = 1, \quad i\rho\left(\frac{\sigma}{k} - U|_{z=0} + \frac{1}{k}\frac{\partial U}{\partial z}\right) = \rho g\varsigma. \tag{A19}$$

Solving (A19) for $\sigma/k - U|_{z=0}$, we get

$$\frac{\sigma}{k} - U|_{z=0} = \left(-\frac{1}{k}\frac{\partial U}{\partial z} \pm \sqrt{\frac{1}{k^2}\left(\frac{\partial U}{\partial z}\right)^2 + 4\frac{g}{k}}\right)\Big/2. \tag{A20}$$

As the mean wavelength is always less than 300 m in our calculation, it is safe to assume $|\partial U/\partial z| \ll \sqrt{4gk}$; then we can expand (A20) to

$$\frac{\sigma}{k} \approx \pm\sqrt{\frac{g}{k}} + U|_{z=0} - \frac{1}{2k}\frac{\partial U}{\partial z} = \pm\sqrt{\frac{g}{k}} + U|_{z=-1/2k}. \tag{A21}$$

Therefore, the apparent phase speed $\sigma / k$ of the wave train is modified by the current speed $U$ (in the direction of the wave propagation) at the depth of $1 / 2k = L / 4\pi$, where $L$ is the wavelength, provided the vertical profile of the mean current is approximately linear. Notice also that the current $V$ perpendicular to the wave direction does not affect the wave phase speed.

## REFERENCES


Bao, J.-W., J. M. Wilczak, J.-K. Choi, and L. H. Kantha, 2000: Numerical simulations of air–sea interaction under high-wind conditions using a coupled model: A study of hurricane development. *Mon. Wea. Rev.,* **128,** 2190–2210.

Bender, M. A., and I. Ginis, 2000: Real-case simulations of hurricane–ocean interaction using a high-resolution coupled model: Effects on hurricane intensity. *Mon. Wea. Rev.,* **128,** 917–946.

——, ——, and Y. Kurihara, 1993: Numerical simulations of tropical cyclone–ocean interaction with a high-resolution coupled model. *J. Geophys. Res.,* **98,** 23 245–23 263.

——, ——, R. Tuleya, B. Thomas, and T. Marchok, 2007: The operational GFDL coupled hurricane–ocean prediction system and a summary of its performance. *Mon. Wea. Rev.,* **135,** 3965–3989.

Black, P. G., and Coauthors, 2007: Air–sea exchange in hurricanes: Synthesis of observations from the Coupled Boundary Layer Air–Sea Transfer experiment. *Bull. Amer. Meteor. Soc.,* **88,** 357–374.

Blumberg, A. F., and G. L. Mellor, 1987: A description of a three-dimensional coastal ocean circulation model. *Three-Dimensional Coastal Ocean Models*, N. S. Heaps, Ed., Amer. Geophys. Union, 1–16.

Canuto, V. M., A. Howard, Y. Cheng, and M. S. Dubovikov, 2001: Ocean turbulence. Part I: One-point closure model—Momentum and heat vertical diffusivities. *J. Phys. Oceanogr.,* **31,** 1413–1426.

Chen, S. S., J. F. Price, W. Zhao, M. A. Donelan, and E. J. Walsh, 2007: The CBLAST-Hurricane program and the next-generation fully coupled atmosphere–wave–ocean models for hurricane research and prediction. *Bull. Amer. Meteor. Soc.,* **88,** 311–317.

Cione, J. J., and E. W. Uhlhorn, 2003: Sea surface temperature variability in hurricanes: Implications with respect to intensity change. *Mon. Wea. Rev.,* **131,** 1783–1796.

Drennan, W. M., H. C. Graber, D. Hauser, and C. Quentin, 2003: On the wave age dependence of wind stress over pure wind seas. *J. Geophys. Res.,* **108,** 8062, doi:10.1029/2000JC000715.

Fan, Y., W. S. Brown, and Z. Yu, 2005: Model simulations of the Gulf of Maine response to storm forcing. *J. Geophys. Res.,* **110,** C04010, doi:10.1029/2004JC002479.

Ginis, I., 2002: Tropical cyclone–ocean interactions. *Atmosphere–Ocean Interactions*, W. Perrie, Ed., Vol. 33, *Advances in Fluid Mechanics*, WIT Press, 83–114.

——, and K. Zh. Dikinov, 1989: Modeling of the Typhoon Virginia (1978) forcing on the ocean. *Sov. Meteor. Hydrol.,* **7,** 53–60.

——, ——, and A. P. Khain, 1989: A three-dimensional model of the atmosphere and the ocean in the zone of a typhoon. *Dokl. Akad. Nauk USSR,* **307,** 333–337.

——, W. Shen, and M. A. Bender, 1999: Performance evaluation of the GFDL coupled hurricane–ocean prediction system in the Atlantic basin. Preprints, *23rd Conf. on Hurricanes and Tropical Meteorology*, Dallas, TX, Amer. Meteor. Soc., 607–610.

Hara, T., and S. E. Belcher, 2002: Wind forcing in the equilibrium range of wind-wave spectra. *J. Fluid Mech.,* **470,** 223–245.

——, and ——, 2004: Wind profile and drag coefficient over mature ocean surface wave spectra. *J. Phys. Oceanogr.,* **34,** 2345–2358.

Holland, G. J., 1980: An analytic model of the wind and pressure profiles in hurricanes. *Mon. Wea. Rev.,* **108,** 1212–1218.

Jacob, S. D., L. K. Shay, A. J. Mariano, and P. G. Black, 2000: The 3D mixed layer response to Hurricane Gilbert. *J. Phys. Oceanogr.,* **30,** 1407–1429.

——, N. Shay, and G. Halliwell, 2005: Evaluation of upper ocean mixing parameterizations. Joint Hurricane Testbed semi-annual Progress Report, 23 pp.

Kenyon, K. E., and D. Sheres, 2006: Wave force on an ocean current. *J. Phys. Oceanogr.,* **36,** 212–221.

Khain, A. P., and I. Ginis, 1991: The mutual response of a moving tropical cyclone and the ocean. *Beitr. Phys. Atmos.,* **64,** 125–141.

Large, W. G., J. C. McWilliams, and S. C. Doney, 1994: Oceanic vertical mixing: A review and a model with nonlocal boundary layer parameterization. *Rev. Geophys.,* **32,** 363–403.

Mellor, G. L., and T. Yamada, 1982: Development of a turbulence closure model for geophysical fluid problems. *Rev. Geophys. Space Phys.,* **20,** 851–875.

Moon, I.-J., I. Ginis, T. Hara, H. Tolman, C. W. Wright, and E. J. Walsh, 2003: Numerical simulation of sea surface directional wave spectra under hurricane wind forcing. *J. Phys. Oceanogr.,* **33,** 1680–1706.

——, T. Hara, I. Ginis, S. E. Belcher, and H. Tolman, 2004a: Effect of surface waves on air–sea momentum exchange. Part I: Effect of mature and growing seas. *J. Atmos. Sci.,* **61,** 2321–2333.

——, I. Ginis, and T. Hara, 2004b: Effect of surface waves on air–sea momentum exchange. Part II: Behavior of drag coefficient under tropical cyclones. *J. Atmos. Sci.,* **61,** 2334–2348.

Morey, S. L., M. A. Bourassa, D. S. Dukhovskoy, and J. J. O'Brien, 2006: Modeling studies of the upper ocean response to a tropical cyclone. *Ocean Dyn.,* **56,** 594–606.

Price, J. F., 1981: Upper ocean response to a hurricane. *J. Phys. Oceanogr.,* **11,** 153–175.

Ren, X., and W. Perrie, 2006: Air–sea interaction of Typhoon Sinlaku (2002) simulated by the Canadian MC2 model. *Adv. Atmos. Sci.,* **23,** 521–530.

Schade, L. R., and K. A. Emanuel, 1999: The ocean's effect on the intensity of tropical cyclones: Results from a simple coupled atmosphere–ocean model. *J. Atmos. Sci.,* **56,** 642–651.

Surgi, N., 2007: Advanced hurricane prediction at NCEP's Environmental Model Center: The operational implementation of the HWRF. *61st Interdepartmental Hurricane Conf.,* New Orleans, LA, Office of the Federal Coordinator for Meteorological Services and Supporting Research (OFCM). [Available online at http://www.ofcm.noaa.gov/ihc07/Presentations/s5-01Surgi-IHC-'07.PPT.]

Tolman, H. L., 2002: User manual and system documentation of WAVEWATCH-III version 2.22. NOAA/NWS/NCEP/MMAB Tech. Note 222, 133 pp.

——, S. H. Hasselmann, H. Graber, R. E. Jensen, and L. Cavaleri, 1996: Application to the open ocean. *Dynamics and Modelling of Ocean Waves,* G. J. Komen et al., Eds., Cambridge University Press, 355–359.

Wright, C. W., and Coauthors, 2001: Hurricane directional wave spectrum spatial variation in the open ocean. *J. Phys. Oceanogr.,* **31,** 2472–2488.